Journal of Power Sources 614 (2024) 234963

Contents lists available at ScienceDirect

Journal of Power Sources

journal homepage: www.elsevier.com/locate/jpowsour

Pressurized single cell testing of solid oxide cells

C. Grosselindemann [a,*], M. Dorn [a], F.M. Bauer [b], M. Seim [a], D. Ewald [a], D. Esau [a], M. Geörg [c], R. Rössler [d], A. Pundt [d], A. Weber [a]

[a] Institute for Applied Materials, Electrochemical Technologies (IAM-ET), Karlsruhe Institute of Technology (KIT), Adenauerring 20b, Karlsruhe, D-76131, Germany
[b] European Institute for Energy Research (EIFER), Emmy-Noether-Straße 11, D-76131, Karlsruhe, Germany
[c] GFS Fuel Cells GmbH, Auf der Trift 3, D-66127, Saarbrücken, Germany
[d] Institute for Applied Materials, Materials Science and Engineering (IAM-WK), Karlsruhe Institute of Technology (KIT), Engelbert-Arnold-Straße 4, Karlsruhe, D-76131, Germany

HIGHLIGHTS

- Highlights (include 3 to 5 bullet points (maximum 85 characters, including spaces, per bullet point)):
- Pressurized operation of SOCs without pressure vessel.
- Glass ceramic sealed SOC gastight up to 11 bar_a.
- Open circuit voltages of up to 1.42 V achieved at 850 °C.
- SOC performance increase of 20 % achieved at 11 bar_a.

ARTICLE INFO

Keywords:
SOC
SOFC
SOEC
Pressurized operation

ABSTRACT

Pressurized operation of Solid Oxide Cells (SOCs) enhances the performance in the fuel cell mode and is mandatory for coupling with gas turbines. For electrolysis, energy demand and balance of plant to pressurize hydrogen or syngas can be reduced. Today's facilities for pressurization of SOCs rely on voluminous pressure vessels that enclose the cells/stacks. Inside such vessel, fuel- and oxidant pressures have to match the vessel pressure to avoid a deterioration of the cells/stacks. Here, a single cell is operated without a pressure vessel in a metallic cell housing sealed towards the cell by a glass-ceramic sealant. Any differential pressure is avoided by a downstream combustor, an approach that is limited to test benches. In our experiments we found that this sealing concept can withstand pressure drops of up to 10 bar towards ambient pressure even after a full thermal cycle. As to be expected from numerous previous studies, open-circuit voltage as well as performance increased significantly with increasing pressure. The power density increased by 20 % in air/dry H_2 at 850 °C and 11 bar_a.

1. Introduction

Solid oxide cells (SOCs) are mostly operated close to atmospheric pressure as the ceramic cells and available high temperature sealants are sensitive towards pressure gradients, which leads to problems regarding gas tightness and pressure regulation [1]. However, it has been known for a long time that pressurized operation of a solid oxide fuel cell (SOFC) enables a higher power density and efficiency. This could be shown in simulative works [2–5] as well as experimentally for single cells [6–9] and stacks [10–13]. The coupling of a SOFC with a gas turbine can further increase the system performance [14–17]. In the case of electrolysis, the produced hydrogen has to be compressed to a level meaningful for the specific application. Mechanical hydrogen compressors are a well-developed technology [18]. However, they still have considerable limitations as they are quite bulky and require a high energy input. Especially the first compression step from ambient pressure to several bar_a (bar_a is used for absolute pressure) is critical. Thus, through bypassing the first compression step for the downstream processes the overall process efficiency can be increased. The coupling of a pressurized SOEC followed by chemical reactor in a power-to-X process has been discussed as a concept and modeling basis in literature [19–21]. However, an experimental coupling of a pressurized SOEC and

* Corresponding author.
E-mail address: cedric.grosselindemann@kit.edu (C. Grosselindemann).

https://doi.org/10.1016/j.jpowsour.2024.234963
Received 15 March 2024; Received in revised form 7 June 2024; Accepted 22 June 2024
Available online 29 June 2024

methanation was so far only shown in the work by Gruber et al. [22].

A detailed theoretical study about the influence of the pressure towards SOC performance and loss mechanisms is provided in literature [23]. Yet experiments under elevated pressure were performed in fuel cell and electrolysis mode. On cell [6–8,24–32] and stack level [11,12,33–36], the operating pressures were mainly set in a range of ~ 1 – 10 bar_a. Limited studies [1] were performed above 10 bar_a. Although, we did find one case with Jensen et al. [13], which operated a stack at pressures as high as 25 bar_a. Generally, the increase of the open-circuit voltage U_{OCV} with increasing pressure is beneficial for fuel cell mode as shown in the work by Henke et al. [37]. The authors stated with the shown improvement of power density, that pressurized operation can decrease costs, weight and volume of SOFC systems as the number of cells can be minimized. Further, Cadigan et al. [11] reported the most significant results in electrochemical performance when operating a SOFC stack with metal-supported cells up to 4 bar_a.

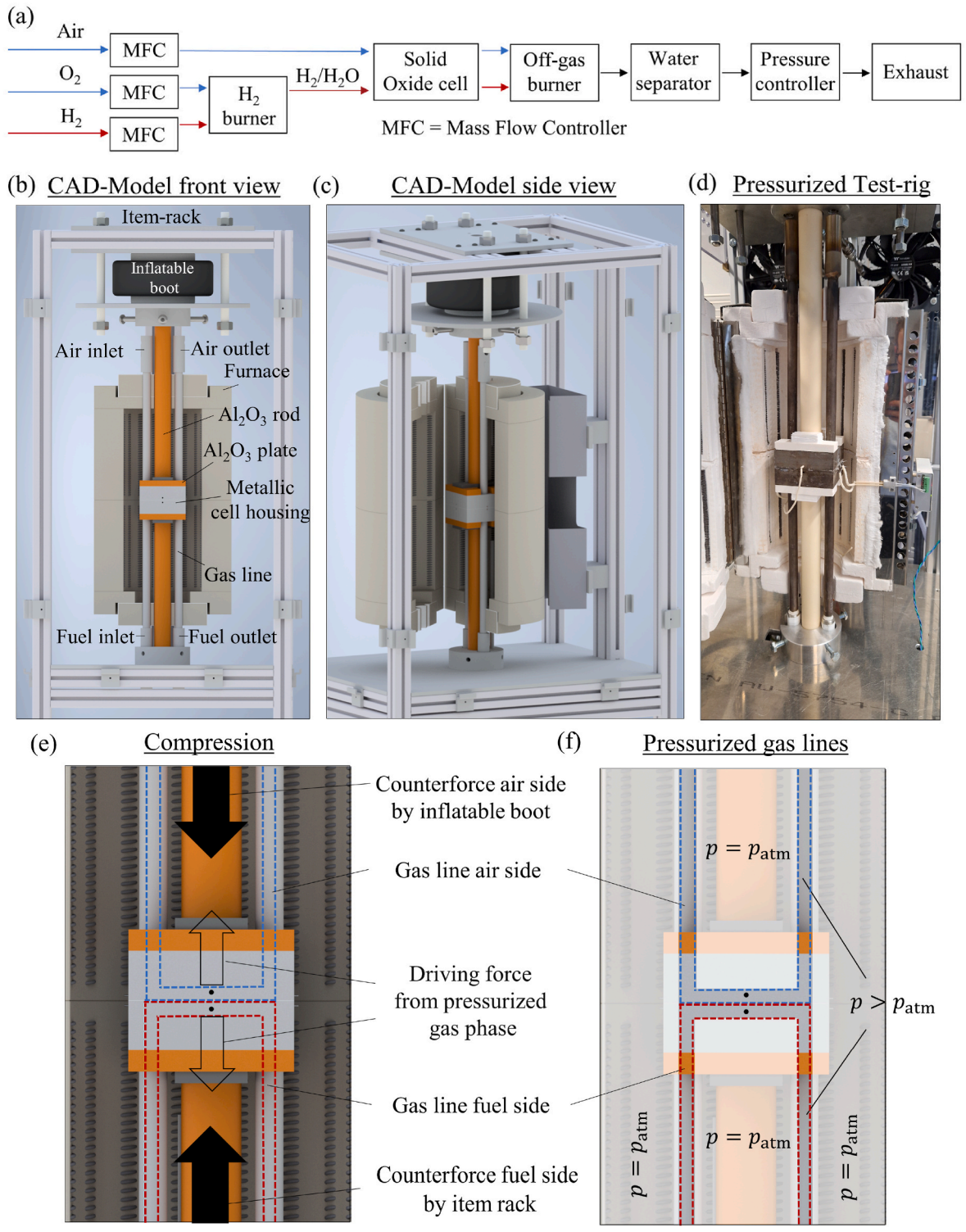

Fig. 1. (a) Flowchart schematic with one pressure regulator only. (b) CAD-model front view as well as (c) side view and (d) view into furnace of pressurized test bench. (e) Schematic compression with inflatable boot and ceramic rods. (f) Scheme of pressurized lines without a pressure vessel.

For electrolysis, an increase in U_{OCV} at higher pressures results in a slightly higher power input. Bernadet et al. [25] and Sun et al. [6] showed with tests of fuel electrode supported cells that this can be leveled out at elevated pressures of up to 10 bar_a and at higher current densities. In the work by Riedel et al. [34] fuel-electrode supported cells were compared in electrolysis mode with electrolyte-supported cells (ESC) on stack level with pressures up to 8 bar_a. It was found, that the stack with ESCs only showed a minor influence towards pressurization. In comparison, for the stack with fuel electrode-supported cells, a performance gain of 3% at 8 bar_a could be achieved. Nevertheless, the authors emphasized that other properties of the cell such as mechanical or redox stability need to be considered for the system design [34].

So far, all known SOC systems and testing devices for cells and stacks were realized with a pressure vessel [1,6,9,13,26,31,32,34–36,38,39], resulting in voluminous, costly and heavy systems. As cells and sealants used in stacks are considered to be limited to pressure gradients in the range of a few hundred $mbar_a$, a complex pressure control strategy is required to align vessel-, fuel- and oxidant pressures. In this work, a SOC is operated at pressures of up to 11 bar_a in a glass-ceramic sealed cell housing without a pressure vessel. A newly developed test bench and metallic cell housing for single cell testing of SOCs with a unique pressure regulation and without external pressure balancing is introduced.

2. Materials and methods

The new test bench is based on existing SOC testing technology [40] that was redesigned to enable pressurized operation without a pressure vessel or complex pressure control strategies. Test bench design, cell dimensions, pressure regulation and electrochemical characterization are described in the following sections.

2.1. Gas supply and pressure regulation

The gas supply is realized via a gas mixing unit as described in Ref. [40]. An upstream combustion chamber is located inside the fuel gas line as can be seen in Fig. 1 (a) (H_2-burner). Here, steam is produced by mixing oxygen to the fuel. This enables up to 100% steam in the fuel gas. A total flow rate of 250 sccm per electrode is set. For reasons of simplicity, atmospheric pressure is assumed to be 1 bar_a in this work. In this test bench a new pressure control concept is applied that is based on a single pressure controller, removing the need to control the differential pressure between fuel and air side as shown in the flowchart schematic in Fig. 1 (a). No further pressure tank is needed in order to balance the pressure. Additionally, in comparison to Ref. [40] here the off-gas from the fuel and air side is united in a downstream combustor as shown in Fig. 1 (a). Thus, only one gas phase is remaining after the off-gas burner. For a reliable, oscillation free operation of the downstream pressure regulator the steam needs to be removed, which is realized by a water separator.

2.2. Pressurized test bench

The pressurized test bench is shown with a CAD-model (designed in Autodesk Inventor Professional 2023) in Fig. 1 (b) with a front view and (c) side view. Further a view inside the furnace is presented in Fig. 1 (d). In comparison to Ref. [40], a metallic cell housing sealed by glass-ceramic sealants is designed. The commonly used fully ceramic set-ups with gold or ceramic sealants are critical regarding gas tightness at elevated pressures. The metallic cell housing is made of APMT (Kanthal® [41]) as this material combines high stability and creep strength under oxidizing and reducing atmospheres with low Cr-evaporation due to the Al_2O_3 oxide scale. The fuel (bottom) and the air side plate (top) of the housing were machined from 30 mm APMT sheets. The APMT gas lines for fuel and air supply inside the furnace are welded to the fuel and air side housing. Fuel and air supply in the plates is realized via milled gas lines schematically shown in Fig. 1(e–f). The metallic housing blocks are compressed between two Al_2O_3-plates by two Al_2O_3 rods (Fig. 1 (e)). The ceramic rods (35 mm in diameter) are fixed at the test rig outside of the furnace. From the top an inflatable boot provides the force for compression in order to withstand the driving force from the gas phase at the electrodes as shown in Fig. 1 (e). Depending on open (unsealed) cell area and operating pressure level this force has to be adjusted. In this study a pressure of 7 bar_a was applied to the inflatable boot corresponding to a force of approx. 8 kN.

2.3. Experimental cells and contacting

Planar electrolyte-supported cells with an active electrode area of 1 x 1 cm^2 were investigated (see Fig. 2 (a)). Even though the APMT is an Al_2O_3-former and thus electrically insulating at the surface, the area of the electrolyte sheet of 10 x 10 cm^2 is equal to the metallic cell housing (see Fig. 2 (g)). This further ensures electrical insulation between the two metallic housing parts. The cells exhibited a Nickel/Gadolinium-Doped Ceria (Ni/GDC) fuel electrode, 3 mol.% yttria-stabilized zirconia (3YSZ) electrolyte substrate and an LSCF air electrode. Additional GDC layers were placed in between electrodes and electrolyte. The microstructure can be observed in a comparable scanning electron microscope (SEM) image as provided in Ref. [42]. Further, a detailed investigation of the electrochemical behavior under atmospheric pressure of this cell type is provided in Ref. [43].

With respect to a contacting, similar to a stack, metallic flow fields were applied and schematically shown in Fig. 2 (b) and (e). A protective coating on the air side is crucial in order to decrease contact losses and achieve an effective blocking of Cr-evaporation [44]. Here, a CeCo coating applied by physical-vapor-deposition was performed by Alleima AB on all sides and edges of the metallic flow field [45–47]. Such a coating can be applied on any ferritic stainless steel grade and is commercialized by Alleima AB (Sanergy™ HT) [48]. The protective layer consists of a top layer of metallic Co with a thickness of approx. 600 nm and a Ce layer in the range of 10 – 20 nm [49]. A detailed description of the contacting set-up and investigation under atmospheric pressures is given in Ref. [50]. The authors showed that this contact set-up minimizes contact losses and blocks Cr-evaporation at the air side effectively.

In Fig. 2 (d) a cross section of the metallic housing is shown with the CAD model. As the Al_2O_3 oxide scale on the APMT-housing is insulating, the metallic flow fields are contacted in a four-point measurement setup via Pt-wires and electrical feedthroughs to ensure a reliable electrical connection. The feedthroughs are realized by platinum wires insulated by Al_2O_3 capillaries towards the metallic housing plates (Fig. 2 (c)). A gas- and pressure tight sealing is realized by silver soldering the capillary and likewise Pt wire into the metallic housing block. An additional ceramic tube is placed inside the APMT fuel gas line, which does not fulfill criteria in terms of sealing but serves as a thermal protective layer with respect to the upstream H_2-burner. The metallic flow fields are placed on exchangeable positioning blocks enabling a high flexibility regarding single cell contacting as shown in Fig. 2 (d) and (e).

Prior to cell mounting, a LSCF contact paste is screen printed onto the air electrode as described in Ref. [50] and shown in Fig. 2 (b). The metallic flow field at the fuel side is in contact with a finely meshed Ni-grid (Fig. 2 (b)). Contact layers at fuel and air side have to provide a sufficient flexibility during mounting. The gas- and pressure tight sealing of the cell is realized by a glass ceramic sealing paste based on the glass powder G018-281 (SCHOTT AG, [51]) that is applied outside the active cell area onto the metallic housing (Fig. 2 (f)) prior to cell mounting. The cell is then placed on the housing in Fig. 2 (g). Afterwards another layer of glass ceramic sealing is applied onto the cell in Fig. 2 (h) to ensure gas tightness between the air side and the metallic cell housing. Thus, the pressurized area in Fig. 2 (i) inside the housing is minimized down to an area of 4.48 cm^2. The resulting sealing width in this setup is 34 to 43 mm, which is significantly larger than a typical sealing width in stacks. A pre-defined thermal protocol for binder burnout and

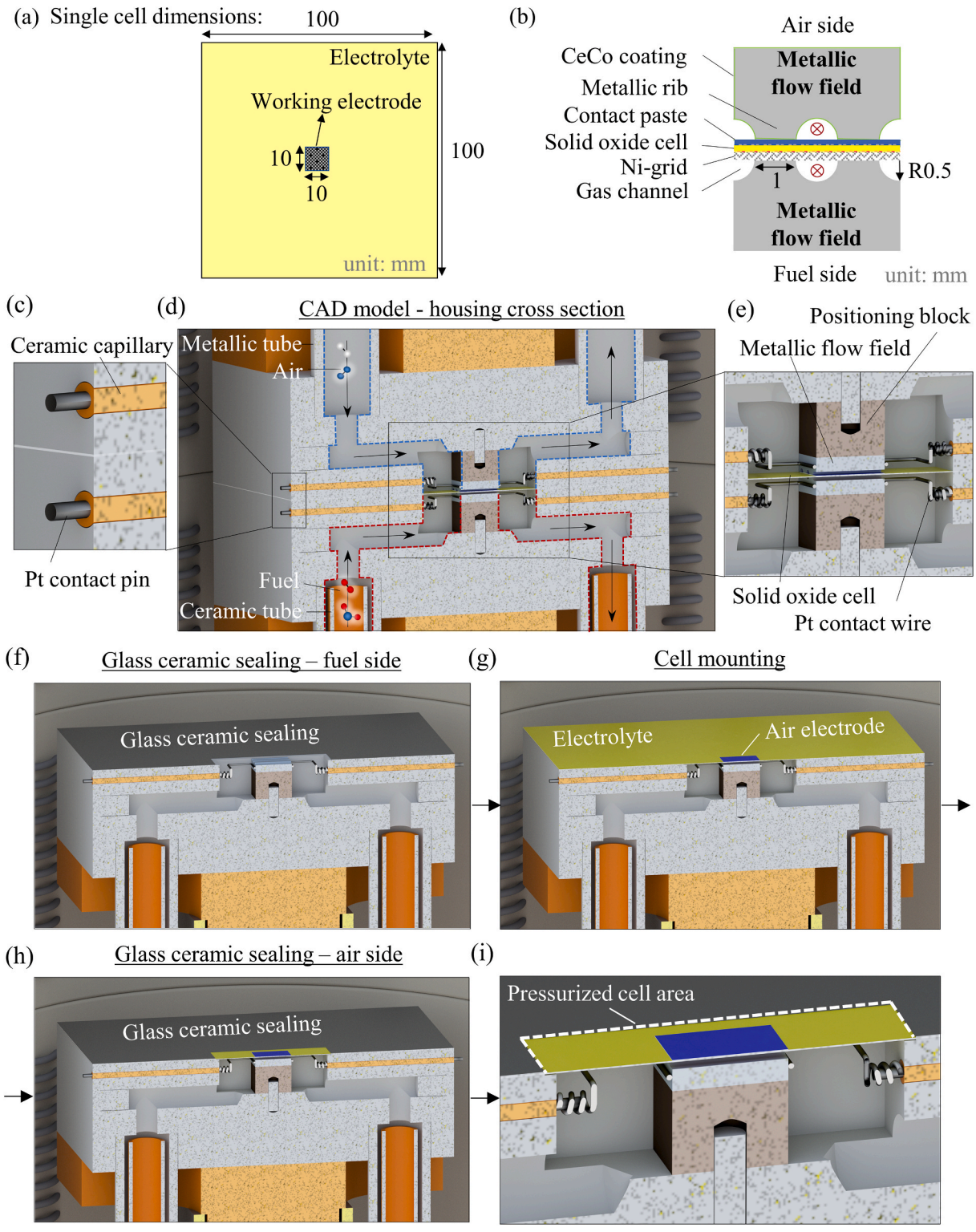

Fig. 2. (a) Single cell dimensions and (b) schematic contacting with metallic flow fields. (c) CAD-model cross section with Pt contact wires in ceramic capillary and (d) CAD model cross-section of metallic cell housing. (e) Stack-like contacting with metallic flow fields, positioning blocks and Pt contact wires. (f) Glass ceramic sealing at the fuel side before mounting the cell in (g). Glass ceramic sealing at the air side in (h) after cell mounting with pressurized cell area in (i).

sealing is performed prior to cell testing.

In the following testing phase, OCV, impedance spectra and IV-characteristics were measured at varied pressures. The spectra were acquired by a Zahner Zennium E frequency response analyzer [40]. The frequency was varied between 30 mHz and 10^5 Hz with 12 points per decade. All spectra were measured under open circuit conditions (OCV). The validity of the spectra was verified by a Kramers Kronig Test [52]. After cell testing and cooling down to ambient temperature, the two metallic housing plates and the cell were still connected by the glass ceramic sealing, which requires further efforts for de-mounting and cleaning of the metallic cell housing. In comparison to the reference test benches exhibiting full ceramic housings and contacting by gold and

Ni-meshes respectively [40], the metallic housing and flow fields and the application of the glass ceramic sealant might affect the cell performance by Cr- or Si-species poisoning the electrode. Effects from the stack-like contacting set-up were discussed in Ref. [50]. Poisoning effects from Si-components from the glass ceramic sealing need to be considered [53] and investigated.

3. Results and discussion

In the following first results of the newly developed pressurized test bench are shown. The effect of pressure towards SOCs is well-known in literature [23] and was demonstrated experimentally in previous works as well [6]. In this work, literature-based knowledge is applied in order to verify the new testing setup.

3.1. N_2 pressure test

Gas tightness of the glass ceramic sealing within the frame of the new pressurized test bench was confirmed with a nitrogen (N_2) pressure test. Here, at 850 °C with 250 sccm N_2 per electrode the pressure was increased stepwise up to 11 bar_a absolute pressure as shown in Fig. 3. After a holding time of 30 min., the gas flow was switched off resulting in a pressure drop of approx. 6 $bar_a\ h^{-1}$. Once the gas flow is switched back on again, the 11 bar_a are reached again after approx. 6 min. This shows sufficient compression and sealing of the cell which was achieved via the inflatable boot and the glass ceramic sealing. Thermal cycling experiments revealed that even after a full thermal cycle the pressure of 11 bar_a could be achieved again. Within the testing phase, the pressure should be changed with a rate of 3 – 5 $mbar_a\ s^{-1}$ to avoid pressure gradients between anode and cathode resulting from different gas volumes and flow rates to both compartments.

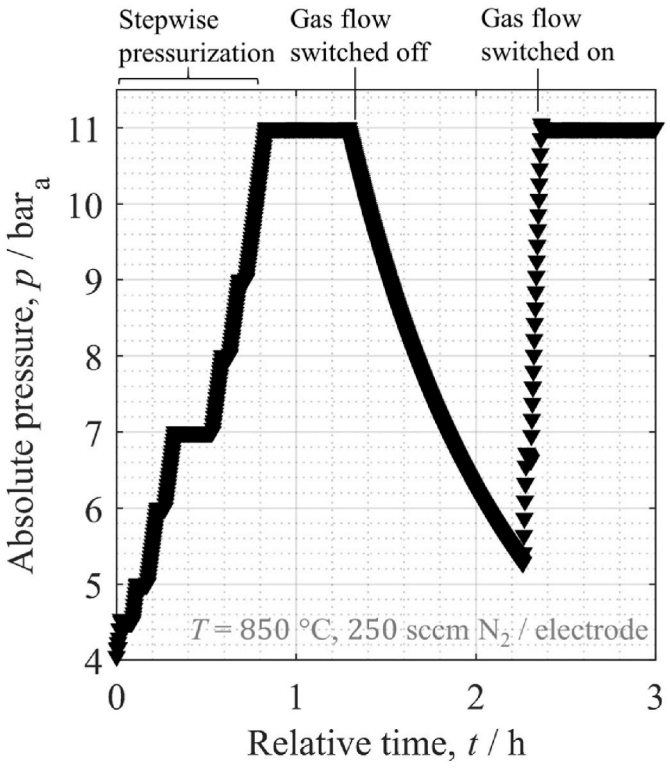

Fig. 3. Pressure test at 850 °C with 100% N_2 and increase of absolute pressure up to 11 bar_a with glass ceramic sealing G018-281.

3.2. Open-circuit voltage

Fig. 4 (a) shows the dependency of the open-circuit voltage as a function of the absolute pressure p at 850 °C with 100% H_2 at the fuel side and synthetic air at the air side. An open-circuit voltage of 1.352 V was reached at atmospheric pressure which corresponds to a leakage of $<$ 0.015% H_2O for measurement #1. The pressure was then increased up to 9 bar_a absolute pressure resulting in an $U_{OCV} = 1.42$ V. By calculation of the Nernst-equation, the measured increase of U_{OCV} can be described in good agreement with a steam content of 0.0125% H_2O and a relative error of $<$ 1%. Considering these comparably low steam contents, the Nernst-equation behaves sensitive to small changes. For measurement #2, the pressure was raised to 11 bar_a with a slightly higher but still tolerable leakage resulting in 0.135% H_2O in the fuel. Here, at pressures above 5 bar_a the deviation from the Nernst-equation increases with a relative error of $<$ 2%. Likewise, this is shown in Fig. 4 (b) for a set fuel gas mixture of 50% H_2 (balance H_2O) and synthetic air at the air side with up to 4 bar_a absolute pressure. The measured voltages correspond to a steam content of 52.5%. This deviation in the steam content most probably originates from an off-set of the flow controllers. The observed impact of pressure on the open-circuit voltage is in good agreement with the Nernst equation and findings in previous studies [6, 23].

3.3. IV-characteristics

First results of IV-characteristics and power density P_{cell} in SOFC mode at 850 °C with 100% H_2 at the fuel side and synthetic air at the air side are shown in Fig. 5 (a). As expected from previous works [6,13], the increase in open-circuit voltage with pressurization is beneficial for SOFC mode as a higher performance is observed with increasing pressure.

The power density P_{cell} at 0.7 V (850 °C with 100% H_2 and synthetic air) is shown in Fig. 5 (b) as a function of the absolute pressure p between 1 – 11 bar_a. In comparison to atmospheric pressure an increase of approx. 20% can be achieved at 11 bar_a regarding a cell voltage of 0.7 V. The major increase of power density was observed between atmospheric conditions and 5 bar_a. The positive impact of pressure on the power density was proved in a number of previous experimental works [10, 37]. In the work by Henke et al. [37] it was also shown, that with an increase of pressure the highest influence can be seen at low pressures. In Fig. 5 (b) the power density with increasing pressure was interpolated according to equation (1) similar to Ref. [37] with the variables A and B. The authors stated a logarithmic behavior of power density with increasing pressure, which was confirmed in this paper in Fig. 5 (b) (goodness of fit: $R^2 = 0.902$).

$$y(x) = A \ln(x) + B \tag{1}$$

Fig. 5 (c) shows the IV-characteristics at 850 °C with 50% H_2 (balance H_2O) and synthetic air at the air side between 1 – 4 bar_a. As expected from the theoretical study [23], the increase of U_{OCV} appears positive for the fuel cell and disadvantageous for electrolysis mode. A higher performance at 4 bar_a can be observed in comparison to atmospheric pressure in fuel cell mode, which is also consistent with previous studies [25,37]. With respect to an electrolyte-supported cell design, the effect of pressure in electrolysis mode is comparably small and similar to findings by Riedel et al. [34].

3.4. Impedance analysis

To evaluate the impact of the stack like contacting, reference measurements at atmospheric pressure were conducted with identical cells and air electrode contacting. Fig. 6 displays impedance spectra and corresponding DRTs for 21% O_2 (balance N_2) and 5% O_2 (balance N_2) at

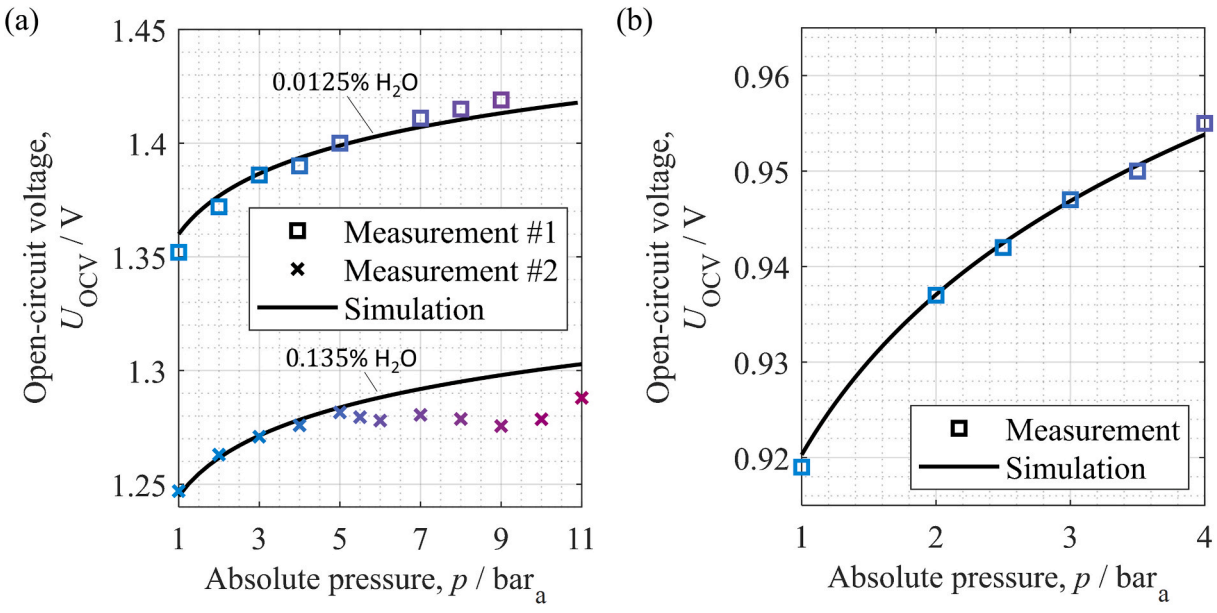

Fig. 4. (a) Measured and simulated OCV as a function of the absolute pressure p with 100% H_2 at the fuel side (simulation with 0.0125% H_2O leakage for measurement #1 and 0.135% H_2O leakage for measurement #2) and synthetic air at the air side at 850 °C. (b) OCV as a function of the absolute pressure with 50% H_2 (balance H_2O, simulation with 52.5% H_2O) and synthetic air at the air side.

the air side and 50% H_2 (balance H_2O) at the fuel side at 850 °C in (a) and (c).

In previous studies [42,43,54] analyzing ideally contacted cells, the different peaks in the DRT were attributed to physicochemical processes. In summary, it was found that P_{LF1} contains overlapping contributions of fuel and air electrode. This includes the surface reaction coupled with ionic transport in superposition with the gas diffusion process at the fuel electrode as well as surface exchange and ionic transport in the air electrode [50,55]. P_{LF2} and P_{HF} were identified as processes related to charge transport in the GDC-phase and at the GDC/YSZ interfaces.

In case of the stack like air electrode contacting, an additional peak P_{LF0} becomes visible (Fig. 6 (a,c)). P_{LF0} and the air electrode contribution to P_{LF1} are both affected by the oxygen partial pressure. An inert gas variation [43,54,56] of the oxidant (Fig. 6 (b,d)) reveals that only P_{LF0} is affected. Thus, P_{LF0} can be attributed to gas diffusion polarization at the air side. In the work by Geisler et al. [57] it was found that in-plane gas diffusion in the contact and cathode layers underneath the ribs of the flow field has a significant impact on cell performance. In order to quantify the impact of gas diffusion in this study, a method from Ref. [54] is adapted. The difference of the polarization resistance ΔR_{pol} (see equation (2)) between the gas mixture with nitrogen R_{pol,N_2} and helium $R_{pol,He}$ is assumed to be equal to the difference of the gas diffusion resistance ΔR_{diff} between the two gas mixtures as shown in Ref. [54].

$$R_{pol,N_2} - R_{pol,He} \equiv R_{diff,N_2} - R_{diff,He} = \Delta R_{diff} \tag{2}$$

Here, the concept of an effective gas diffusion parameter G_{eff} is adapted to the air electrode (equation (3)). Ψ_{AE} denotes the microstructure parameter and L_{AE} an averaged gas diffusion length.

$$G_{eff,AE} = \frac{\Psi_{AE}}{L_{AE}} \tag{3}$$

The gas diffusion resistance at the air side $R_{diff,AE}$ can be calculated according to equation (4) with $\tilde{R}$ denoting the universal gas constant, T the temperature, F the faraday constant, D_{O_2} the binary gas diffusion coefficient, $y_{O_2,AE}$ the molar fraction of oxygen and P_{corr} an conversion factor 10^5 Pa bar_a^{-1}. Based on Ref. [58], molecular combined with Knudsen gas diffusion is considered. Thus, D_{O_2} is based on the Bosanquet-approach and the molecular gas diffusion coefficient D_{mol,O_2} is calculated by Chapman-Enskog [59].

$$R_{diff,AE} = \left(\frac{\tilde{R}T}{4F}\right)^2 \bullet \frac{1}{G_{eff,AE}} \bullet \frac{1}{D_{O_2} \bullet p}\left(\frac{1}{y_{O_2,AE}} - 1\right) \bullet \frac{1}{P_{corr}} \tag{4}$$

On the basis of equations (2)–(4) the effective gas diffusion parameter can be determined with equation (5) resulting in $G_{eff,AE} = 188.74$ m^{-1} with a $\Delta R_{pol} = 21.8$ mΩ cm^2 in Fig. 6 (b).

$$G_{eff,AE} = \left(\frac{\tilde{R}T}{4F}\right)^2 \bullet \frac{1}{\Delta R_{diff}} \bullet \frac{1}{p}\left(\frac{1}{y_{O_2,AE}} - 1\right)\left(\frac{1}{D_{O_2,N_2}} - \frac{1}{D_{O_2,He}}\right) \bullet \frac{1}{P_{corr}} \tag{5}$$

The first impedance measurements of pressurized testing with the new test bench are presented in Fig. 7 (a) with the distribution of relaxation times in Fig. 7 (b). The spectra were measured at 850 °C with 50% H_2 (balance H_2O) and synthetic air at the air side at pressures of 1 and 4 bar_a.

The increase in pressure results in a decrease of the ohmic resistance by about 5 mΩ cm^2. Here, a number of effects discussed in literature might have contributed to this behavior. In the work by Momma et al. [8], a decrease of the ohmic resistance with increasing pressure was reported and attributed to the conductivity of the air electrode material [60] and a lower contact resistance between air electrode and current collector. Previous investigations [50] of the stack like contacting revealed a contact resistance of 13 mΩ cm^2, which might decrease at higher pressures. Further, the conductivity in the GDC bulk in the fuel

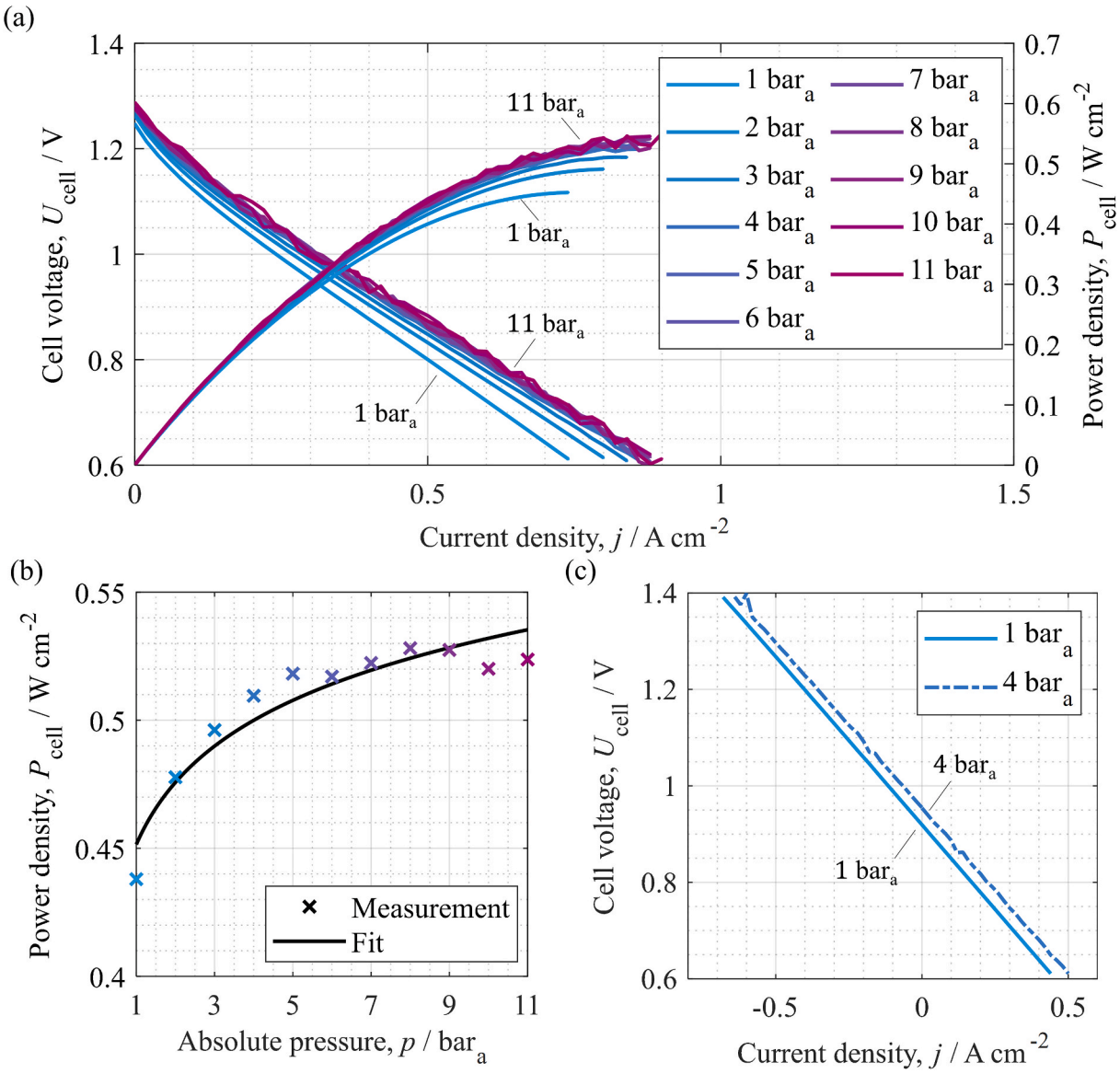

Fig. 5. (a) IV-characteristics and power density P_{cell} in SOFC-mode at 850 °C with 100% H_2 and synthetic air at the air side between 1 – 11 bar$_a$. (b) Power density P_{cell} as a function of the absolute pressure p at 850 °C with 100% H_2/synthetic air at 0.7 V with logarithmic fit. (c) IV-characteristics at 850 °C with 50% H_2 (balance H_2O) and synthetic air at the air side between 1 – 4 bar$_a$.

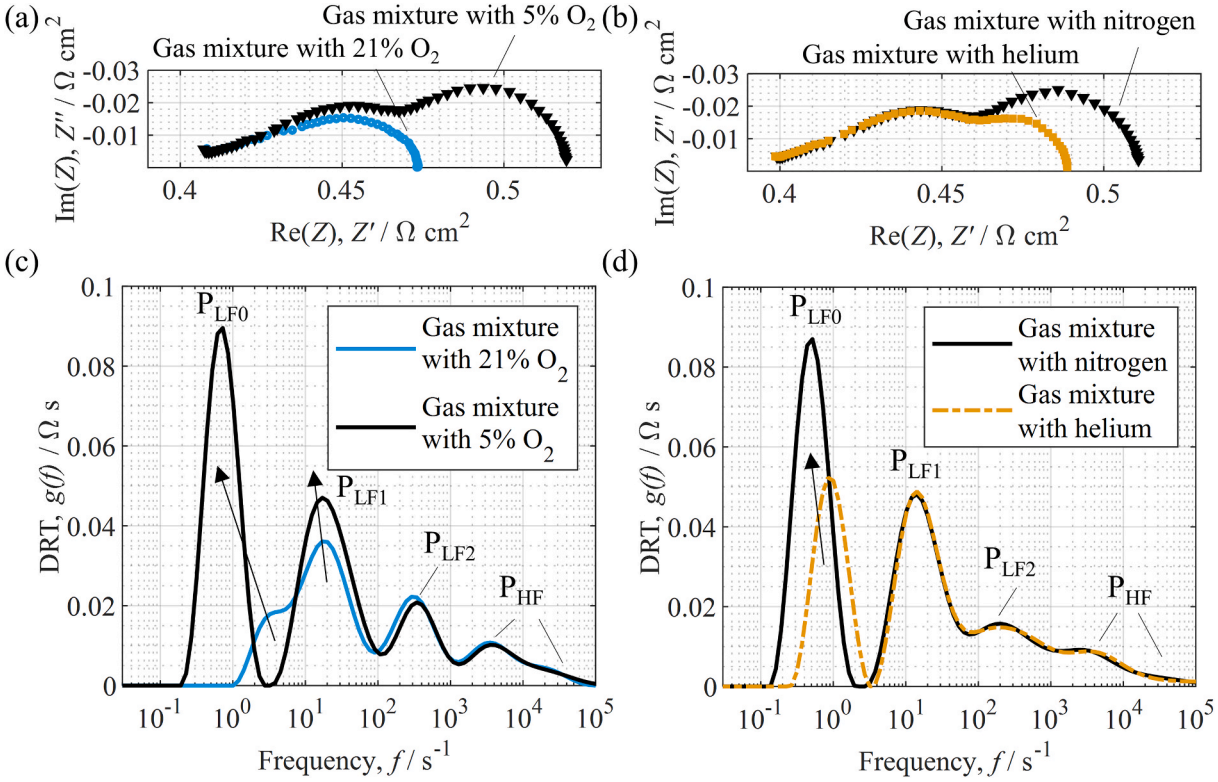

Fig. 6. Impedance spectra of a stack like contacted cell at atmospheric pressure in (a) for 21% O_2 (balance N_2) and 5% O_2 (balance N_2) at the air side and with 50% H_2 (balance H_2O) at the fuel side at 850 °C with corresponding DRT in (c). Impedance spectra at atmospheric pressure in (b) with 5% O_2 (balance N_2 or He) at the air side and with 50% H_2 (balance H_2O) at the fuel side at 850 °C with corresponding DRT in (d).

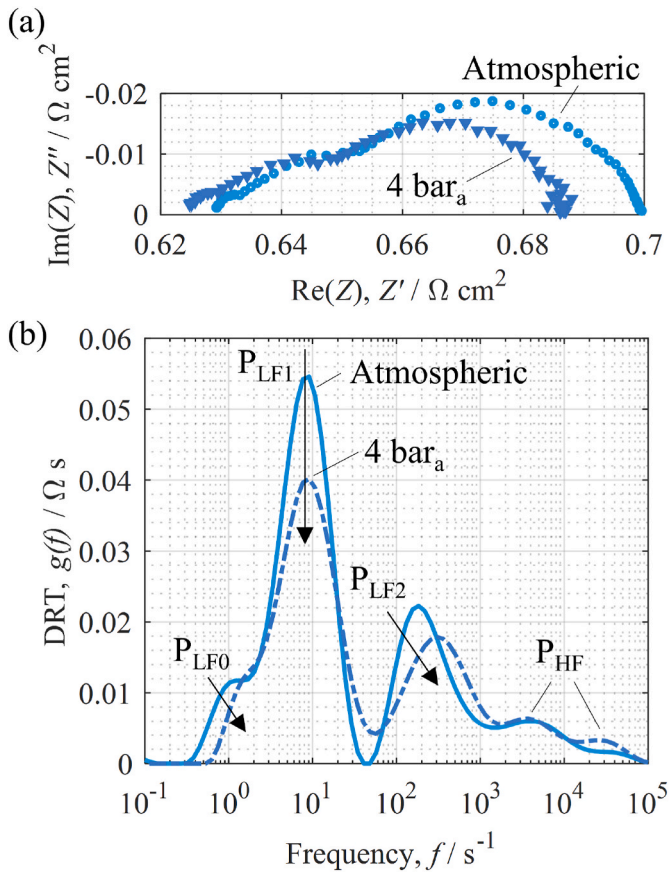

Fig. 7. (a) Impedance spectra and (b) DRT at 850 °C with 50% H_2 (balance H_2O) and synthetic air at the air side between 1 bar_a and 4 bar_a.

influenced. The conductivity of GDC is depending on the oxygen partial pressure. Based on Wang et al. [61] the impact at the air side is assumed to be neglectable since at comparably higher oxygen partial pressures no significant change in conductivity can be observed. Regarding the fuel electrode, the oxygen partial pressure calculated with Cantera [62] at 850 °C and 50% H_2 (balanced with H_2O) is independent of pressure and thus no impact from here is expected. Additionally, the conductivity of the oxide scale of the metallic flow field exhibiting a Co–Mn spinel layer [50,63] may play a comparably larger role here. This needs to be investigated in more detail in future work.

The polarization resistance is decreasing by approx. 8 mΩ cm^2, which can be related to reduced activation and/or gas diffusion polarization resistances [6]. At first, the impact of pressure on the gas diffusion process at the air side P_{LF0} is discussed. The gas diffusion resistances at atmospheric pressure ($R_{diff,AE,atm} = 9.4$ mΩ cm^2) and 4 bar_a ($R_{diff,AE,4bar_a} = 6.9$ mΩ cm^2) are calculated with the help of equation (4), revealing a difference of 2.5 mΩ cm^2 that is contributing to the decrease in the overall polarization resistance.

The peak P_{LF1} in Fig. 7 (b) at approx. 10 Hz is mostly affected by the change in pressure. In Refs. [2,23] it was shown that the gas diffusion regime determines the impact of pressure regarding the electrochemical behavior. In comparison to the air side, here a finely meshed Ni-grid is applied for contacting. Thus, based on a previous work [54] gas diffusion in the porous fuel electrode structure with molecular and Knudsen gas diffusion was neglected due to the small electrode thickness. Instead a gas diffusion layer above the electrode with pure molecular gas diffusion inside the contact mesh and gas channel can be assumed at the fuel side. In this case the molecular gas diffusion coefficient is inversely proportional to the absolute pressure ($D_{mol,i} \sim p^{-1}$). In equation (6) the gas diffusion resistance [64] at the fuel electrode (FE) is shown with the molar fractions of hydrogen $y_{H_2,FE}$ and steam $y_{H_2O,FE}$. By inserting the molecular gas diffusion coefficient in equation (6), the impact of pressure is leveled out and the resulting gas diffusion resistance $R_{diff,FE}$ at the fuel side is independent of pressure.

Table 1
Model parameters of a solid oxide cell with Ni/GDC fuel electrode, 3YSZ electrolyte and LSCF air electrode extracted from Ref. [54].

Parameter	Unit	Value
$E_{act,FE}$	kJ mol^{-1}	90.54
$a(T = 850°C)$	–	0.161
$b(T = 850\,°C)$	–	0.359
$\gamma_{FE}(T)$	A m^{-2}	$1.46 \bullet 10^5 (A\,m^{-2}K^{-1}) \bullet [0.8^a \bullet 0.2^b]^{-1} \bullet T$
$E_{act,AE}$	kJ mol^{-1}	144.54
m	–	0.42
$\gamma_{AE}(T)$	A m^{-2}	$5.47 \bullet 10^9 (A\,m^{-2}K^{-1}) \bullet T$

electrode and within the GDC interlayer at the air side may be

Table 2
List of physical processes at fuel and air electrode with corresponding frequency range and indication of pressure dependency.

Peak	Frequency range	Physical process		Pressure dependency
–	[Hz]	Fuel electrode	Air electrode	–
P_{LF0}	0.5 – 3	–	Gas diffusion	Yes
P_{LF1}	3 – 30	Surface reaction coupled with ionic transport in the GDC phase, overlap with gas diffusion [43]	Oxygen surface exchange coupled with O^{2-} diffusion in the bulk of the air electrode [55]	Yes
P_{LF2}	30 – 2000	Ionic transport in the GDC phase coupled with surface reactions + interfacial processes [43]	Dominated by O^{2-} diffusion in the bulk of the air electrode coupled with oxygen surface exchange [55]	Yes
P_{HF}	> 2000	Interfacial and bulk processes [43]	Non-surface related processes, possibly resistive interfacial processes [54]	No

$$R_{\mathrm{diff,FE}} = \left(\frac{\widetilde{R}T}{2F}\right)^2 \bullet \frac{L_{\mathrm{FE}}}{\Psi_{\mathrm{FE}}} \bullet \frac{1}{p} \bullet \left(\frac{1}{D_{\mathrm{mol,H_2}} \bullet y_{\mathrm{H_2,FE}}} + \frac{1}{D_{\mathrm{mol,H_2O}} \bullet y_{\mathrm{H_2O,FE}}}\right) \frac{1}{P_{\mathrm{corr}}} \tag{6}$$

Subsequently, the impact of pressure on P_{LF1} should solely result from a decrease of the activation polarization at the fuel and/or air electrode. The activation resistance $R_{act,el}$ for the electrodes (*el*) is provided in equation (7). Here, $j_{0,el}$ denotes the exchange current density of the electrodes. It's dependency on the pressures is shown in equations (8) and (9) for fuel and air electrode respectively.

$$R_{\mathrm{act},el} = \frac{1}{j_{0,el}} \bullet \frac{\widetilde{R}T}{2F} \tag{7}$$

$$j_{0,\mathrm{FE}} = \gamma_{\mathrm{FE}} \left(\frac{y_{\mathrm{H_2,FE}} \bullet p}{p_{\mathrm{ref}}}\right)^a \left(\frac{y_{\mathrm{H_2O,FE}} \bullet p}{p_{\mathrm{ref}}}\right)^b \exp\left(-\frac{E_{\mathrm{act,FE}}}{\widetilde{R}T}\right) \tag{8}$$

$$j_{0,\mathrm{AE}} = \gamma_{\mathrm{AE}} \left(\frac{y_{\mathrm{O_2,AE}} \bullet p}{p_{\mathrm{ref}}}\right)^m \exp\left(-\frac{E_{\mathrm{act,AE}}}{\widetilde{R}T}\right) \tag{9}$$

The dependency of the exchange current density becomes obvious and can be calculated. The required parameters γ_{el}, a, b, m and $E_{act,el}$ were determined in a previous study [54] under atmospheric pressure and are summarized in Table 1.

Based on this, the activation resistance at the fuel side is calculated for atmospheric pressure ($R_{act,FE,atm} = 37.5$ mΩ cm^2) as well as at 4 bar$_a$ ($R_{act,FE,4\ bar_a} = 18.2$ mΩ cm^2). This results in a difference of 19.2 mΩ cm^2. As shown in Ref. [54], the activation resistance at the air side is neglectable under atmospheric pressure at 850 °C and air at the air side. The calculated impact of pressure towards the activation resistance is larger than the measured value of 8 mΩ cm^2 minus the gas diffusion at the air electrode of 2.5 mΩ cm^2. However, the model parameters were determined at atmospheric pressure and might not be valid for higher pressures. Processes underneath P_{LF2} seem to be affected with pressure as well, which may result from the coupling of P_{LF1} and P_{LF2} in a transmission line model. Processes above 10^3 Hz (P_{HF}) do not seem to be impacted by increasing pressure as they are related to bulk processes.

Based on this analysis the physicochemical backgrounds of the DRT-peaks and their pressure dependencies are summarized in Table 2.

4. Conclusions

In this paper, we present first results obtained with a newly developed testing concept enabling pressurized operation of solid oxide cells without a pressure vessel. The cells were sealed in a metal housing by a glass ceramic sealant that enabled pressurization of fuel and air compartments up to 11 bar$_a$. Differential pressures between the fuel and air sides are ruled out by a new pressure regulation concept. A downstream off-gas burner unites fuel and oxidant flow, which enables a simplified pressure control in contrast to overly complex differential pressure control strategies. The glass-ceramic sealed metal housing enabled pressure variations between atmospheric and 11 bar$_a$ as well as thermal cycling without mechanical failure. The single cell tests revealed an excellent sealing of the cell enabling OCV values of up to 1.42 V. The pressure dependency of the OCV was in excellent agreement with the Nernst-equation. The expected impact of pressure on the cell performance was confirmed, IV-characteristics in the SOFC-mode showed an increase in power density of up to 20%. In the SOEC-mode the expected increase in voltage, resulting in higher electrical power demands, were confirmed as well. Impedance spectra showed the expected decrease of the different polarization processes at elevated pressure. Finally, the ohmic resistance showed a decrease that requires further analysis.

Nomenclature

latin letters	
a	Exponent describing hydrogen partial pressure dependency of the fuel electrode's exchange current density (−)
b	Exponent describing steam partial pressure dependency of the fuel electrode's exchange current density (−)
D_i	Gas diffusion coefficient of the component i (m^2 s^{-1})
$D_{\mathrm{mol},i}$	Molecular gas diffusion coefficient of the component i (m^2 s^{-1})
E_{act}	Activation energy (J mol^{-1})
F	Faraday constant (As mol^{-1})
G_{eff}	Effective gas diffusion parameter (m^{-1})
$j_{0,El}$	Exchange current density (A m^{-2})
m	Exponent describing oxygen partial pressure dependency of the air electrode's exchange current density (−)
p	Absolute pressure (bar$_a$)
p_{ref}	Reference pressure = 1.013 bar$_a$
P_{cell}	Power density (W m^{-2})
P_{corr}	Conversion factor 10^5 (Pa bar$_a^{-1}$)
$\widetilde{R}$	Universal gas constant 8.314 (J mol^{-1} K^{-1})
R_{diff}	Gas diffusion resistance (Ω m^2)
R_{pol}	Polarization resistance (Ω m^2)
R_{act}	Activation resistance (Ω m^2)
ΔR_{diff}	Difference of the gas diffusion resistance (Ω m^2)
ΔR_{pol}	Difference of the polarization resistance (Ω m^2)
T	Temperature (K)
t	Time (s)
U_{OCV}	Open circuit voltage (V)
U_{cell}	Cell voltage (V)
y	Molar fraction (−)
greek letters	
γ	Exponential pre-factor (A m^{-2})
δ	Concentration of oxygen lattice vacancy (−)
Ψ	Microstructure parameter (−)
subscripts	
cell	Cell
corr	Correction
diff	Gas diffusion
eff	Effective
EL	Electrode
H_2	Hydrogen
H_2O	Steam
He	Helium
N_2	Nitrogen
OCV	Open-circuit voltage
pol	Polarization
abbreviations	
Al_2O_3	Aluminum oxide
GDC	Gadolinium-Doped Ceria
DRT	Distribution of relaxation times
H_2	Hydrogen
H_2O	Steam
LSCF	$La_wSr_xCo_yFe_zO_{3-\delta}$
MFC	Mass Flow Controller
N_2	Nitrogen
O_2	Oxygen
OCV	Open-circuit-voltage
SOC	Solid oxide cell
SOEC	Solid oxide electrolyzer cell
SOFC	Solid oxide fuel cell
3YSZ	3 mol.% yttria-stabilized zirconia

CRediT authorship contribution statement

C. Grosselindemann: Writing – original draft, Methodology, Investigation, Formal analysis, Data curation, Conceptualization. **M. Dorn:** Software, Methodology, Conceptualization. **F.M. Bauer:** Methodology, Conceptualization. **M. Seim:** Investigation, Conceptualization. **D. Ewald:** Investigation, Writing – review & editing. **D. Esau:** Investigation, Writing – review & editing. **M. Geörg:** Methodology, Conceptualization. **R. Rössler:** Methodology. **A. Pundt:** Writing – review & editing, Supervision, Investigation. **A. Weber:** Writing – review & editing, Supervision, Project administration, Methodology, Investigation, Funding acquisition, Conceptualization.

Declaration of competing interest

The authors declare that they have no known competing financial interests or personal relationships that could have appeared to influence the work reported in this paper.

Data availability

Data can be found under the DOI: 10.35097/1971.

Acknowledgments

The authors gratefully acknowledge funding from the Helmholtz Society Innovation Pool project "Solar hydrogen: high purity and compressed" (38.03.02) and from the Federal Ministry of Education and Research in the project H2Giga-HTEL-Stacks (BMBF 03HY124C). Sincere thanks are given to Sunfire GmbH for producing the test cells. Alleima AB made the coating for the metallic interconnectors gratefully available. Special thanks are given to Ralf Rössler for welding the APMT housing parts and tubes. Glass ceramic sealings were gratefully provided by the SCHOTT AG. The LSCF contact paste was thankfully provided by Norbert Menzler from Forschungszentrum Jülich GmbH, Institute of Energy and Climate Research (IEK), IEK-1: Materials Synthesis and Processing. We also would like to thank Martin Deichelbohrer for his fruitful assistance in CAD drawing and Daniel Kesler for proof-reading this paper.

References

[1] J. Brabandt, O. Posdziech, System approach of a pressurized high-temperature electrolysis, ECS Trans. 78 (2017) 2987, https://doi.org/10.1149/07801.2987ecst.
[2] M. Henke, J. Kallo, K.A. Friedrich, W.G. Bessler, Influence of pressurisation on SOFC performance and durability: a theoretical study, Fuel Cell. 11 (2011) 581–591, https://doi.org/10.1002/fuce.201000098.
[3] Y. Wang, R. Zhan, Y. Qin, G. Zhang, Q. Du, K. Jiao, Three-dimensional modeling of pressure effect on operating characteristics and performance of solid oxide fuel cell, Int. J. Hydrogen Energy 43 (2018) 20059–20076, https://doi.org/10.1016/j.ijhydene.2018.09.025.
[4] W. Jiang, R. Fang, J.A. Khan, R.A. Dougal, Parameter setting and analysis of a dynamic tubular SOFC model, J. Power Sources 162 (2006) 316–326, https://doi.org/10.1016/j.jpowsour.2006.06.086.
[5] K.P. Recknagle, E.M. Ryan, B.J. Koeppel, L.A. Mahoney, M.A. Khaleel, Modeling of electrochemistry and steam–methane reforming performance for simulating pressurized solid oxide fuel cell stacks, J. Power Sources 195 (2010) 6637–6644, https://doi.org/10.1016/j.jpowsour.2010.04.024.
[6] X. Sun, A.D. Bonaccorso, C. Graves, S.D. Ebbesen, S.H. Jensen, A. Hagen, P. Holtappels, P.V. Hendriksen, M.B. Mogensen, Performance characterization of solid oxide cells under high pressure, Fuel Cell. 15 (2015) 697–702, https://doi.org/10.1002/fuce.201500020.
[7] L. Zhou, M. Cheng, B. Yi, Y. Dong, Y. Cong, W. Yang, Performance of an anode-supported tubular solid oxide fuel cell (SOFC) under pressurized conditions, Electrochim. Acta 53 (2008) 5195–5198, https://doi.org/10.1016/j.electacta.2008.02.032.
[8] A. Momma, K. Takano, Y. Tanaka, T. Kato, A. Yamamoto, Experimental investigation of the effect of operating pressure on the performance of SOFC and SOEC, ECS Trans. 57 (2013) 699, https://doi.org/10.1149/05701.0699ecst.
[9] Y.D. Hsieh, Y.H. Chan, S.S. Shy, Effects of pressurization and temperature on power generating characteristics and impedances of anode-supported and electrolyte-supported planar solid oxide fuel cells, J. Power Sources 299 (2015) 1–10, https://doi.org/10.1016/j.jpowsour.2015.08.080.
[10] S. Seidler, M. Henke, J. Kallo, W.G. Bessler, U. Maier, K.A. Friedrich, Pressurized solid oxide fuel cells: experimental studies and modeling, J. Power Sources 196 (2011) 7195–7202, https://doi.org/10.1016/j.jpowsour.2010.09.100.
[11] C. Cadigan, C. Chmura, G. Floerchinger, P. Frankl, S. Hunt, S. Jensen, C. Boushehri, T.L. Vincent, R. Braun, N.P. Sullivan, Performance characterization of metal-supported solid-oxide fuel cell stacks at elevated pressure, J. Power Sources 573 (2023) 233083, https://doi.org/10.1016/j.jpowsour.2023.233083.
[12] A.A. Burke, L.G. Carreiro, J.R. Izzo, Pressurized testing of a planar solid oxide fuel cell stack, Int. J. Hydrogen Energy 38 (2013) 13774–13780, https://doi.org/10.1016/j.ijhydene.2013.08.058.
[13] S.H. Jensen, X. Sun, S.D. Ebbesen, M. Chen, Pressurized operation of a planar solid oxide cell stack, Fuel Cell. 16 (2016) 205–218, https://doi.org/10.1002/fuce.201500180.
[14] R.A. George, Status of tubular SOFC field unit demonstrations, J. Power Sources 86 (2000) 134–139, https://doi.org/10.1016/S0378-7753(99)00413-9.
[15] Y. Kobayashi, Y. Ando, H. Kishizawa, K. Tomida, N. Matake, Recent progress of SOFC-gt combined system with tubular type cell stack at MHI, ECS Trans. 51 (2013) 79, https://doi.org/10.1149/05101.0079ecst.
[16] S.E. Veyo, S.D. Vora, K.P. Litzinger, W.L. Lundberg, Status of Pressurized SOFC/Gas Turbine Power System Development at Siemens Westinghouse, American Society of Mechanical Engineers Digital Collection, 2009, pp. 823–829, https://doi.org/10.1115/GT2002-30670.
[17] K. Tanaka, C. Wen, K. Yamada, Design and evaluation of combined cycle system with solid oxide fuel cell and gas turbine, Fuel 79 (2000) 1493–1507, https://doi.org/10.1016/S0016-2361(99)00293-8.
[18] G. Sdanghi, G. Maranzana, A. Celzard, V. Fierro, Review of the current technologies and performances of hydrogen compression for stationary and automotive applications, Renew. Sustain. Energy Rev. 102 (2019) 150–170, https://doi.org/10.1016/j.rser.2018.11.028.
[19] L.R. Clausen, G. Butera, S.H. Jensen, High efficiency SNG production from biomass and electricity by integrating gasification with pressurized solid oxide electrolysis cells, Energy 172 (2019) 1117–1131, https://doi.org/10.1016/j.energy.2019.02.039.
[20] G. Butera, S.H. Jensen, R.Ø. Gadsbøll, J. Ahrenfeldt, L.R. Clausen, Biomass conversion to methanol integrating solid oxide cells and two-stage gasifier: effects of carbon dioxide recirculation and pressurized operation, Chemical Engineering Transactions 76 (2019) 1177–1182, https://doi.org/10.3303/CET1976197.
[21] L. Wehrle, D. Schmider, J. Dailly, A. Banerjee, O. Deutschmann, Benchmarking solid oxide electrolysis cell-stacks for industrial Power-to-Methane systems via hierarchical multi-scale modelling, Appl. Energy 317 (2022) 119143, https://doi.org/10.1016/j.apenergy.2022.119143.
[22] M. Gruber, P. Weinbrecht, L. Biffar, S. Harth, D. Trimis, J. Brabandt, O. Posdziech, R. Blumentritt, Power-to-Gas through thermal integration of high-temperature steam electrolysis and carbon dioxide methanation - experimental results, Fuel Process. Technol. 181 (2018) 61–74, https://doi.org/10.1016/j.fuproc.2018.09.003.
[23] M. Henke, C. Willich, J. Kallo, K.A. Friedrich, Theoretical study on pressurized operation of solid oxide electrolysis cells, Int. J. Hydrogen Energy 39 (2014) 12434–12439, https://doi.org/10.1016/j.ijhydene.2014.05.185.
[24] R. Kikuchi, T. Yano, T. Takeguchi, K. Eguchi, Characteristics of anodic polarization of solid oxide fuel cells under pressurized conditions, Solid State Ionics 174 (2004) 111–117, https://doi.org/10.1016/j.ssi.2004.05.029.
[25] L. Bernadet, G. Gousseau, A. Chatroux, J. Laurencin, F. Mauvy, M. Reytier, Influence of pressure on solid oxide electrolysis cells investigated by experimental and modeling approach, Int. J. Hydrogen Energy 40 (2015) 12918–12928, https://doi.org/10.1016/j.ijhydene.2015.07.099.
[26] G. Hughes, J. Railsback, D. Butts, S.A. Barnett, Electrochemical performance of solid oxide cell oxygen electrodes under pressurization, ECS Trans. 68 (2015) 687, https://doi.org/10.1149/06801.0687ecst.
[27] S.S. Shy, S.C. Hsieh, H.Y. Chang, A pressurized ammonia-fueled anode-supported solid oxide fuel cell: power performance and electrochemical impedance measurements, J. Power Sources 396 (2018) 80–87, https://doi.org/10.1016/j.jpowsour.2018.06.006.
[28] S.C. Singhal, Recent progress in tubular solid oxide fuel cell technology, SAVE Proc. 1997–40 (1997) 37, https://doi.org/10.1149/199740.0037PV.
[29] Y. Luo, Y. Shi, Y. Chen, W. Li, L. Jiang, N. Cai, Pressurized tubular solid oxide H2O/CO2 coelectrolysis cell for direct power-to-methane, AIChE J. 66 (2020) e16896, https://doi.org/10.1002/aic.16896.
[30] M.T. Mehran, S.-B. Yu, D.-Y. Lee, J.-E. Hong, S.-B. Lee, S.-J. Park, R.-H. Song, T.-H. Lim, Production of syngas from H2O/CO2 by high-pressure coelectrolysis in tubular solid oxide cells, Appl. Energy 212 (2018) 759–770, https://doi.org/10.1016/j.apenergy.2017.12.078.
[31] Q. Cacciuttolo, J. Vulliet, V. Lair, M. Cassir, A. Ringuedé, Influence of pressure on the electrical and electrochemical behaviour of high-temperature steam electrolyser La0.6Sr0.4Co0.2Fe0.8O3 anode, J. Solid State Electrochem. 22 (2018) 3663–3671, https://doi.org/10.1007/s10008-018-4048-2.
[32] C. Herradon, L. Le, C. Meisel, J. Huang, C. Chmura, Y.D. Kim, C. Cadigan, R. O'Hayre, N.P. Sullivan, Proton-conducting ceramics for water electrolysis and hydrogen production at elevated pressure, Front. Energy Res. 10 (2022). https://www.frontiersin.org/articles/10.3389/fenrg.2022.1020960. (Accessed 18 December 2023).
[33] S.H. Jensen, C. Graves, M. Chen, J.B. Hansen, X. Sun, Characterization of a planar solid oxide cell stack operated at elevated pressure, J. Electrochem. Soc. 163 (2016) F1596, https://doi.org/10.1149/2.1171614jes.
[34] M. Riedel, M.P. Heddrich, A. Ansar, Q. Fang, L. Blum, K.A. Friedrich, Pressurized operation of solid oxide electrolysis stacks: an experimental comparison of the performance of 10-layer stacks with fuel electrode and electrolyte supported cell concepts, J. Power Sources 475 (2020) 228682, https://doi.org/10.1016/j.jpowsour.2020.228682.
[35] M. Tomberg, M.P. Heddrich, M. Metten, S.A. Ansar, K.A. Friedrich, Operation of a solid oxide fuel cell reactor with multiple stacks in a pressured system with fuel gas recirculation, Energy Technol. 10 (2022) 2101075, https://doi.org/10.1002/ente.202101075.
[36] J.E. O'Brien, X. Zhang, G.K. Housley, K. DeWall, L. Moore-McAteer, High Temperature Electrolysis Pressurized Experiment Design, Operation, and Results, Idaho National Lab. (INL), Idaho Falls, ID (United States), 2012, https://doi.org/10.2172/1056004.
[37] M. Henke, C. Willich, C. Westner, F. Leucht, R. Leibinger, J. Kallo, K.A. Friedrich, Effect of pressure variation on power density and efficiency of solid oxide fuel cells, Electrochim. Acta 66 (2012) 158–163, https://doi.org/10.1016/j.electacta.2012.01.075.

[38] L. Bernadet, J. Laurencin, G. Roux, D. Montinaro, F. Mauvy, M. Reytier, Effects of pressure on high temperature steam and carbon dioxide Co-electrolysis, Electrochim. Acta 253 (2017) 114–127, https://doi.org/10.1016/j.electacta.2017.09.037.
[39] Q. Cacciuttolo, J. Vulliet, V. Lair, M. Cassir, A. Ringuedé, Effect of pressure on high temperature steam electrolysis: model and experimental tests, Int. J. Hydrogen Energy 40 (2015) 11378–11384, https://doi.org/10.1016/j.ijhydene.2015.04.034.
[40] D. Klotz, A. Weber, E. Ivers-Tiffée, Practical guidelines for reliable electrochemical characterization of solid oxide fuel cells, Electrochim. Acta 227 (2017) 110–126, https://doi.org/10.1016/j.electacta.2016.12.148.
[41] Kanthal® APMT — Kanthal®, (n.d.). https://www.kanthal.de/produkte-und-dienstleistungen/material-datasheets/tube/kanthal-apmt/(accessed June 7, 2024).
[42] F. Kullmann, C. Grosselindemann, L. Salamon, F.-M. Fuchs, A. Weber, Impedance analysis of electrolyte processes in a solid oxide cell, Fuel Cell. 23 (2023), https://doi.org/10.1002/fuce.202300035.
[43] D. Esau, C. Grosselindemann, S. Sckuhr, F. Kullmann, A. Lindner, Z. Liang, F.-M. Fuchs, A. Weber, Electrochemical characterization of Nickel/gadolinia doped Ceria fuel electrodes under H2/H2O/CO/CO2-atmospheres, J. Electrochem. Soc. (2024), https://doi.org/10.1149/1945-7111/ad4c10.
[44] N.H. Menzler, D. Sebold, Q. Fang, Chromium-related degradation of thin-film electrolyte solid oxide fuel cell stacks, J. Electrochem. Soc. 162 (2015) F1275, https://doi.org/10.1149/2.0101512jes.
[45] N. Norrby, S. Li, M. Stenström, J. Westlinder, The coating effect on interconnect materials after >10 Years of furnace exposures, ECS Trans. 111 (2023) 2223, https://doi.org/10.1149/11106.2223ecst.
[46] C. Goebel, V. Asokan, S. Khieu, J.-E. Svensson, J. Froitzheim, Self-healing properties of Ce/Co-coated stainless steel under simulated intermediate temperature solid oxide fuel cell conditions, Surf. Coating. Technol. 428 (2021) 127894, https://doi.org/10.1016/j.surfcoat.2021.127894.
[47] M.J. Reddy, J.-E. Svensson, J. Froitzheim, Reevaluating the Cr evaporation characteristics of Ce/Co coatings for interconnect applications, ECS Trans. 103 (2021) 1899, https://doi.org/10.1149/10301.1899ecst.
[48] SanergyTM HT, (n.d.). https://www.alleima.com/en/products/coated-strip-steel/sanergy-ht/(accessed June 7, 2024).
[49] C. Bernuy-Lopez, U. Bexell, M. Stenstrom, N. Norrby, J. Westlinder, The time for industrialization has come: a pre-coated solution for the gw scale, ECS Trans. 103 (2021) 1803, https://doi.org/10.1149/10301.1803ecst.
[50] C. Grosselindemann, M.J. Reddy, H. Stormer, D. Esau, M. Dorn, F.M. Bauer, D. Ewald, L. Wissmeier, J. Froitzheim, A. Weber, Impact of CeCo-coated metallic interconnectors on SOCs towards performance, Cr-Oxide-Scale, and Cr-evaporation, J. Electrochem. Soc. (2024), https://doi.org/10.1149/1945-7111/ad44da.
[51] SCHOTT Festoxid-Elektrolyseurzellen (SOEC), (n.d.). https://www.schott.com/de-de/expertise/anwendungen/festoxid-elektrolyseurzellen (accessed December 15, 2023).
[52] M. Schönleber, D. Klotz, E. Ivers-Tiffée, A method for improving the robustness of linear kramers-kronig validity tests, Electrochim. Acta 131 (2014) 20–27, https://doi.org/10.1016/j.electacta.2014.01.034.
[53] R. Kiebach, K. Agersted, P. Zielke, I. Ritucci, M.B. Brock, P.V. Hendriksen, A novel SOFC/SOEC sealing glass with a low SiO2 content and a high thermal expansion coefficient, ECS Trans. 78 (2017) 1739, https://doi.org/10.1149/07801.1739ecst.
[54] C. Grosselindemann, N. Russner, S. Dierickx, F. Wankmüller, A. Weber, Deconvolution of gas diffusion polarization in Ni/Gadolinium-Doped Ceria fuel electrodes, J. Electrochem. Soc. 168 (2021) 124506, https://doi.org/10.1149/1945-7111/ac3d02.
[55] A. Leonide, V. Sonn, A. Weber, E. Ivers-Tiffée, Evaluation and modeling of the cell resistance in anode-supported solid oxide fuel cells, J. Electrochem. Soc. 155 (2007) B36, https://doi.org/10.1149/1.2801372.
[56] V. Sonn, A. Leonide, E. Ivers-Tiffée, Combined deconvolution and CNLS fitting approach applied on the impedance response of technical Ni / 8YSZ cermet electrodes, J. Electrochem. Soc. 155 (2008) B675, https://doi.org/10.1149/1.2908860.
[57] H. Geisler, A. Kromp, A. Weber, E. Ivers-Tiffée, Stationary FEM model for performance evaluation of planar solid oxide fuel cells connected by metal interconnectors: I. Model framework and validation, J. Electrochem. Soc. 161 (2014) F778, https://doi.org/10.1149/2.079406jes.
[58] J. Joos, Microstructural characterisation, modelling and simulation of solid oxide fuel cell cathodes. https://doi.org/10.5445/KSP/1000064791, 2017.
[59] B.E. Poling, J.M. Prausnitz, J.P. O'connell, The Properties of Gases and Liquids, Mcgraw-hill, New York, 2001. https://www.academia.edu/download/62015682/Prausnitz_-_Properties_of_Gases_and_Liquids20200206-55970-35et18.pdf. (Accessed 29 May 2024).
[60] S. Wang, M. Katsuki, M. Dokiya, T. Hashimoto, High temperature properties of La0.6Sr0.4Co0.8Fe0.2O3−δ phase structure and electrical conductivity, Solid State Ionics 159 (2003) 71–78, https://doi.org/10.1016/S0167-2738(03)00027-4.
[61] S. Wang, T. Kobayashi, M. Dokiya, T. Hashimoto, Electrical and ionic conductivity of Gd-doped Ceria, J. Electrochem. Soc. 147 (2000) 3606.
[62] D.G. Goodwin, H.K. Moffat, I. Schoegl, R.L. Speth, B.W. Weber, Cantera: an object-oriented software toolkit for chemical kinetics, thermodynamics, and transport processes. https://www.cantera.org, 2022.
[63] M.J. Reddy, T.E. Chausson, J.E. Svensson, J. Froitzheim, 11–23% Cr steels for solid oxide fuel cell interconnect applications at 800 °C – how the coating determines oxidation kinetics, Int. J. Hydrogen Energy (2023), https://doi.org/10.1016/j.ijhydene.2022.11.326.
[64] S. Primdahl, M. Mogensen, Gas diffusion impedance in characterization of solid oxide fuel cell anodes, J. Electrochem. Soc. 146 (1999) 2827, https://doi.org/10.1149/1.1392015.